PAPER • **OPEN ACCESS**

A novel body centered cubic 3D auxetic chiral geometry

OPEN ACCESS
IOP Publishing
Smart Materials and Structures
Smart Mater. Struct. **34** (2025) 015050 (18pp)
https://doi.org/10.1088/1361-665X/ad9dc9

A novel body centered cubic 3D auxetic chiral geometry

Antonio Maria Caporale[1,*], **Alessandro Airoldi**[1] **and Nejc Novak**[2]

[1] Aerospace Science and Technology Department, Politecnico di Milano, Via La Masa 34, 20156 Milano, Italy
[2] Faculty of Mechanical Engineering, University of Maribor, Maribor, Smetanova ul. 17, 2000 Maribor, Slovenia

E-mail: antoniomaria.caporale@polimi.it

Received 27 September 2024, revised 29 November 2024
Accepted for publication 11 December 2024
Published 24 December 2024

Abstract

Auxetic materials and structures have a negative Poisson's ratio (PR), which means that they expand under a longitudinal tensile loading and shrink under compressive load. This property gives them an increased shear resistance, damping and energy absorption capabilities. Chiral geometries are among the most effective auxetic structures for their ability to convert the axial loading in the rotation of their internal nodes. In the present work, a novel 3D chiral geometry is presented, and its response is investigated both experimentally and numerically. It is made of spheres placed following a Body Centered Cubic lattice; each one connected to the closest neighbors by eight ligaments. A sample was 3D-printed and mechanically tested in compression exhibiting an auxetic behavior in certain directions. A Finite Element model was then developed, successfully reproducing the outcome of the experimental tests, both in terms of force and PR. Then, a numerical testing campaign was performed on representative units constrained using periodic boundary conditions. This campaign allows to evaluate the mechanical properties of the structure as a function of its geometrical parameters. It shows to be able to exhibit an approach a PR of -1 in all the directions. Moreover, the relationship between the sphere's rotation, PR and instability was investigated.

Keywords: three-dimensional auxetics, chiral, negative Poisson's ratio, instability

1. Introduction

Cellular and meta-materials, which have internal cellular structure on a nano, micro, meso, or macro size, are among the most promising multifunctional materials with cutting-edge features for future engineering applications [1]. The unusual and desirable combination of their mechanical and thermal properties is made possible by combining different base materials with the specifically constructed internal cellular structure of various morphologies [2]. Individual requirements can be met by carefully designing the cellular structure's geometry and introducing graded porosity [3]. Additionally, it is possible to construct the cellular structure so that it has a negative Poisson's ratio (PR) under external loading, which causes the structure to expand laterally under longitudinal tensile loading and compressively under compressive loading [4–8]. This behavior was observed on different length scale, from the molecular one [9, 10], passing through the crystalline one [11], to the meso-scale of the foam cells [4], to the macro-scale. It is made possible by the carefully designed 2D or 3D hinge-like cellular skeleton with predefined shape [12–18], even with a certain degree of disorder [19, 20]. The negative PR cellular materials are also called auxetic meta-materials and

* Author to whom any correspondence should be addressed.

they greatly improve mechanical properties in particular cases, in several technical, medicinal, fashion, textile, and sports applications [21]. The increased shear efficiency of the auxetic materials (increased shear modulus) was also reported [22]. Moreover, they show efficient mechanical damping, acoustic insulation [23] (also with band gaps control [24]) and energy absorption [25–28] capabilities. The auxetic cellular structures also have a consistent and predictable fatigue behavior [29, 30] which allow the crack propagation path to be predefined [31]. They are increasingly being investigated as sandwich panel cores for impact protection for body and vehicle armor applications as lightweight multifunctional components [32–35].

Chiral structures are a class of topologies which in certain conditions can show auxetic behavior. A certain geometry can be called chiral if it is non-superimposable on its mirror image, which means that it has two distinct forms, called enantiomers. A typical example of it are the human hands; for this reason, the two enantiomers are usually referred to as 'right-handed' and 'left-handed', respectively. From a mathematical point of view, in a two-dimensional space, a chiral structure does not have any axis of symmetry; in a three-dimensional space, a chiral structure does not have any plane of symmetry or center of symmetry. One of the most famous chiral structures which exhibit an auxetic behavior is the one presented by Prall and Lakes [36]. It is made of straight ligaments (ribs or struts) joined to center nodes, which are typically circles or other geometric shapes. The auxetic effects of this variety of chiral auxetic structures are accomplished by wrapping or unwrapping the ligaments around the nodes in response to the applied force. Theoretical and practical studies demonstrate that the chiral structures' PR can approach values close to -1 in the elastic deformation range [37]. Different version of Lakes configuration with different number of ligaments [38] or different tessellation [39–42] exhibit auxetic behavior. The experimental testing of various chiral auxetic structures under tensile and bending loading was reported in [43, 44]. The elastic properties of chiral honeycombs in transverse direction were analytically determined in [45], while the dynamic and impact loading of sandwich panel with chiral core was studied and experimentally tested [46]. The experimental testing and computational simulations of chiral auxetic structures were also used for the evaluation of possible applications in morphing wings [47, 48] and localized impact [28, 49]. Spadoni *et al* compared analytical calculations with results of finite element (FE) simulations in [50], where good agreement was achieved in the case of compression testing of chiral structures. The results were compared to the conventional and re-entrant honeycombs, where it was concluded that the chiral structures offer more considerable specific buckling stiffness. Similar was also proven in the study by Miller *et al* where tetra and hexachiral structures were analyzed using analytical, experimental, and computational methods [51].

In recent years, several three-dimensional auxetic geometries were proposed [2], based on different mechanisms, such as reentrant cells [52–55], axisymmetric [55–57] double arrowhead [58], triply periodic minimal surfaces [59–61], and rotating units [62, 63]. Different geometries belonging to a specific class of 3d sphere-based structures were proposed, which coupling the spheres displacement and rotation [64], in some case with an anti-chiral pattern [65, 66], in some cases with a fully chiral topology [67–69], or in some case triggered by the instabilization of the ligaments [70, 71], lead to peculiar mechanical behaviors. Negative PR was achieved in anti-chiral topologies, as well as in some of the instability modes of the sphere-based structures. On the other hand, in fully chiral sphere-based structure a significatively negative PR was never achieved.

In the present work, a novel three-dimensional chiral structure is presented and its auxetic behavior is investigated. The purpose of this study is primarily to illustrate the development of the structure, its behavior, and the effect of the variation of the geometrical parameters. Nonetheless, this work allowed us to observe and enlighten the similarities and the differences between two- and three-dimensional chiral structures, the link between the rotations of internal units, with the auxetic behavior of the structure and its stability. Its geometrical concept is based on spheres repeated in space with a body centered cubic (BCC) periodicity. The spheres are then connected to their first neighbors by ligaments, with a chiral pattern which favors a unique axis of rotation. A sample of this structure was produced using 3D printed and subjected to static compression tests in different directions. A numerical FE model of the experimental compression tests was developed and validated. Then, different configurations of the structure are investigated, using a FE model of a representative unit with periodic boundary conditions (PBCs), varying the geometrical parameters and studying their influence on stiffness, PR and stability, exploring the relationship between sphere rotation, auxeticity and instability. Moreover, the application of the method here presented is just an example of the many possible three-dimensional auxetic configurations based on spheres and ligament.

2. Geometrical concept

In their work, Prall and Lakes [36] presented a two-dimensional chiral pattern that can have PRs of ≈ -1 (figure 1(a)), typically referred to as hexachiral. Variations of this pattern with different number of ligaments were then defined [38] (figure 1(b)). Auxetic behavior is obtained due to the coupling of the in-plane displacement of the nodes and their in-plane rotation. This coupling is caused by the chiral disposition of the ligaments, which exert a system of reaction forces on the rings not equilibrated to that rotation. A micropolar description of this behavior was presented in [37].

The structure presented in this work is, for some aspects, a three-dimensional generalization of this chiral pattern, in which the circular nodes are replaced by spheres, placed following as a BCC lattice, connected to their eight first neighbors by four ligaments. To obtain an appreciable auxetic behavior, a displacement-rotation coupling of the sphere can be induced with a chiral disposition of the ligaments, as in the 2D case. In the 2D case, the rotation axis of each node can be easily

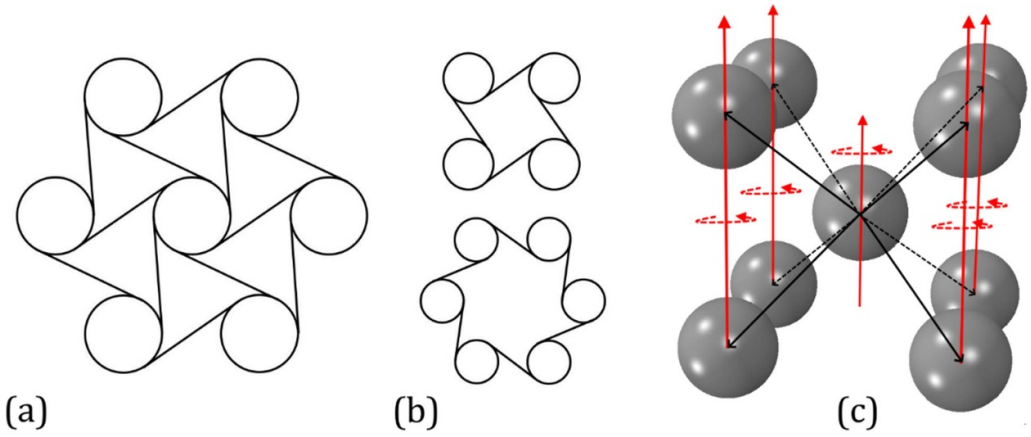

Figure 1. (a) Hexachiral auxetic pattern presented by Prall and Lakes [36], (b) two variations with four and three ligaments [38], and (c) BCC cell of with nine spheres and the favorable rotation axis of each of them.

identified as the out-of-plane one, passing through the center of the node itself; in the 3D case, the number of possible axes is infinite. This issue was investigated in [67], in which a similar, fully chiral, simple cubic structure was developed. In this work, it was shown how the presence of infinite possible axes of rotation hinders any displacement-rotation coupling, leading to a PR which hardly goes negative. Moreover, infinite possible rotation axes cause infinite deformation mode in response to a certain applied load, making the structure easily prone to instability. For this reason, in this work the possible auxetic behavior of a structure with a single favorable rotation axis was investigated. For the sake of simplicity, the ligaments were arranged in such a way that all the rotation axes of all the spheres are parallel and that they are subjected to a rotation with the same sign, as shown in figure 1(c).

Once all the rotation axes and sign were defined, the disposition of the ligaments was designed to maximize the displacement-rotation coupling. As in the 2D case, the optimal solution is having the ligaments tangentially connecting to the node/sphere surface. Thus, a first representative unit was designed, composed of a sphere and eight half-ligaments connected to it. The process to define the disposition of the ligaments is shown in figure 2. It started with a sphere of radius r inscribed in a cube with side L, where the sphere and the cube are concentric and $r \leqslant L/2$, so that the sphere volume is completely included inside the cube, as shown in figure 2(a). The eight half-ligaments, here idealized as lines, were defined by connecting the eight vertices of the cube with the sphere's surface, respecting two conditions: the position of the eight connection points on the sphere surface must have a certain regularity and they must be placed such that the ligaments are tangent to the sphere surface. The first condition can be satisfied by inscribing another cube with side equal to $l = 2/\sqrt{3} \cdot r$ inside the sphere, so that they are concentric; then, the vertices of the internal cube will be on the sphere's surface and they can be used together with the eight vertices of the external cube to define the eight half-ligaments (figure 2(b)). The second condition, the tangency of the half-ligaments, can be satisfied by rotating the inscribed cube around the vertical axis of an angle θ, defined as:

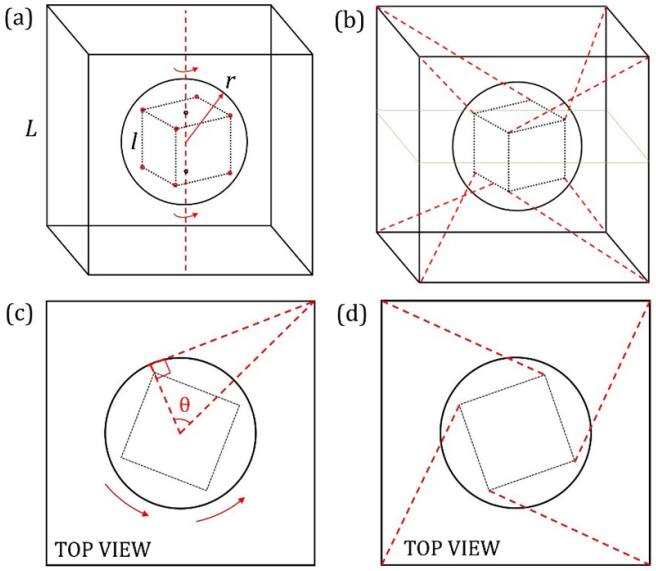

Figure 2. Development of the BCC chiral fundamental element: (a) a sphere and two cubes, one containing the sphere and one inscribed in the sphere, all concentric, (b) the ligaments which connect the vertices of the external and internal cubes, (c) the projection on the top view (normal to the favored rotation axis) of the angle θ between the inner and the outer cube, and (d) the chiral disposition of the ligaments.

$$\theta = \cos^{-1}\left(\frac{2r}{\sqrt{2}L}\right) \tag{1}$$

This formula was derived from simple geometrical considerations, and it gives two angles as a solution, equal in magnitude but opposite in sign. By choosing the same angle for each half-ligament, the disposition shown in figure 2(d) is obtained. It must be underlined that this representative unit is not chiral, since it is symmetrical with respect to the horizontal plane passing through the center of the sphere (see figure 2(b)). The disposition of the ligaments is nonetheless based on a two-dimensional chiral pattern as it can be seen from the top view (figure 2(d)).

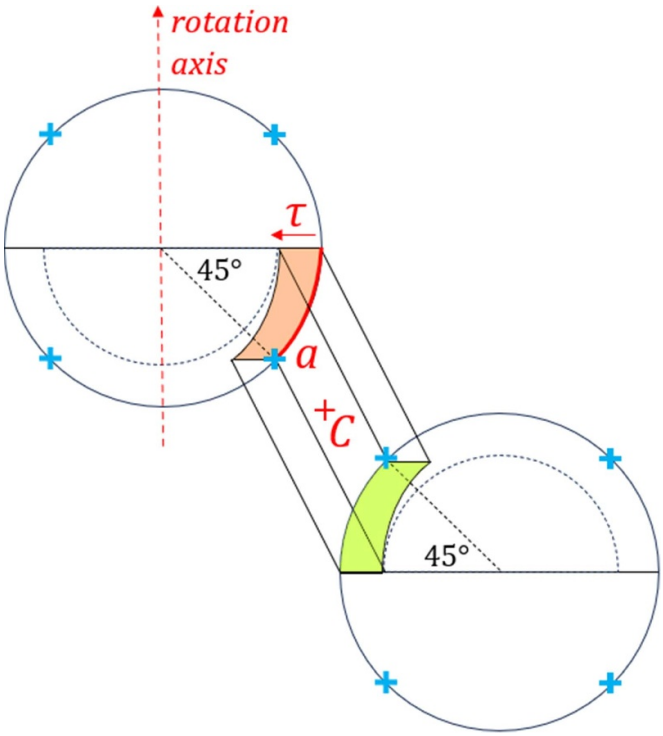

Figure 3. Schematics of the morphology of a ligament connecting two neighboring spheres.

Once the ligaments disposition was defined, the real ligaments were shaped. This process is illustrated in figure 3. To do that, a 45° arc of a circle a (in red in figure 3) was defined on the meridian plane passing through one of the connection points defined before (marked in blue in figure 3). This arc joins the connection point to the closer equatorial plane. A second arc of a circle was obtained by translating the first one along the radius of the sphere of a length τ. In this way, a flat surface was defined (in orange in figure 3). Let us define point C as the midpoint of the line joining the centers of two neighboring spheres. By applying a central symmetry with respect to point C to this surface, a second surface is obtained on the second sphere (in green in figure 3). By linearly connecting these two surfaces, geometry of ligament was obtained. Two observations must be made: the first is that the ligament section variates along its length. It starts as a 45° arc with a length of $\frac{\pi r}{4}$ extruded by a length of τ, to become a parallelogram with a width of $2r \cdot \sin\left(\frac{\pi}{16}\right)$ extruded by τ, in the middle section. Thus it depends only on τ and r. The second observation is that the thickness of the ligament is not constant and is not equal to the extrusion length τ.

The resulting fundamental element is shown in figure 4(a). The structure defined can be fully described by a set of three parameters, represented in figure 4: D is the distance between two neighboring spheres, t is the minimum ligament thickness, and r is the sphere radius. Then, the t/D ratio and the r/D ratio are the ligament thickness and spheres radius normalized to the spheres distance. To move from the fundamental element to a finite BCC structure, three further parameters are needed, namely the three primitive orthogonal translation vectors v_x, v_y and v_z, to be applied to a basis made of two fundamental elements, as shown in figure 4(b). In figure 4(c), the detail of the actual geometry of a ligament is shown, while a schematic representation of the process of translations of the basis in the lattice is shown in figure 4(d).

The lattice was then built by applying the set of translations V, which can be written as:

$$V = a \cdot v_x + b \cdot v_y + c \cdot v_z \tag{2}$$

where a, b, and c are integers and, for a cubic lattice, $v_x = v_y = v_z$ and $v_x \perp v_y \perp v_z$. In figure 5(a), a BCC cell is shown with the three translation vectors. Considering this geometry, it can be assumed that in the xy plane, the structure presents a square symmetry, which means that given a certain property ψ it is invariant to the $\pi/2$ rotations around the z axis:

$$\psi(0) = \psi\left(k\frac{\pi}{2}\right) \text{ where } k = 0,\ 1,\ 2,\ 3,\ldots \tag{3}$$

This means that the properties in the direction x and y are the same. Thus, it is useful to define a further axis s, defined by the vector $[1,1,0]$ in the reference system shown in figure 5(a).

An example of a structure with a, b, and c ranging from 1 to 4 is shown in figure 5(b). Then, all the spheres with less than four ligaments were removed to obtain a more compact and robust structure (figure 5(c)). Observing the structure from the top, a tetrachiral pattern can be recognized, even if the spheres lay on different planes (figure 5(d)). In the same way, observing the structure from the direction of the longer diagonal, an hexachiral pattern can be recognized (figure 5(e)).

3. Experimental methods

3.1. Manufacturing

A structure like the one in figure 5(c) was 3D-printed using multi jet fusion (MJF) technique by a commercial company using a HP 5210 Pro printer. HP 3D HR PA 12 Nylon 12 was used for its strength and toughness to avoid unwanted failures of the ligaments during the testing. The quality of specimens obtained in this way was widely described in [72–74]. The geometrical parameters which define the structure are reported in table 1. The 3D-printed structure is shown in figure 6, from the top and the lateral view.

3.2. Compression tests

Static compression tests were performed to verify and quantify the auxetic behavior of the structure. The tests were performed using an MTS 810 material testing system, which acquired the displacement of the crosshead and the reaction force with a sampling frequency of 10 Hz, in environmental temperature and humidity conditions. The specimen was compressed between two flat surfaces, as shown in figure 6, where a thin layer of grease was sprayed to lower the effects of the friction. The crosshead velocity was set to 0.5 mm min^{-1}. The external spheres were painted black and white dots were drawn on their faces to track their displacement. The two colors were chosen

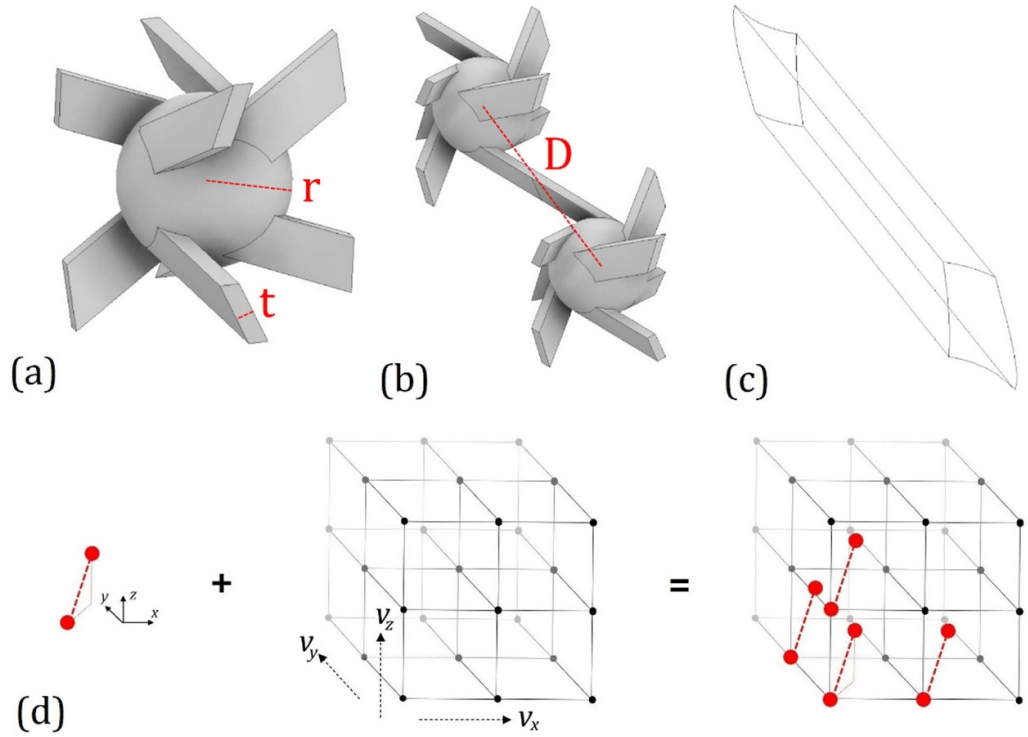

Figure 4. (a) Fundamental element of the BCC chiral structure, (b) the two-spheres basis of the structure, (c) the actual ligament geometry, (d) and schematic representation of the translation of the basis in the points of a cubic lattice to create the BCC lattice.

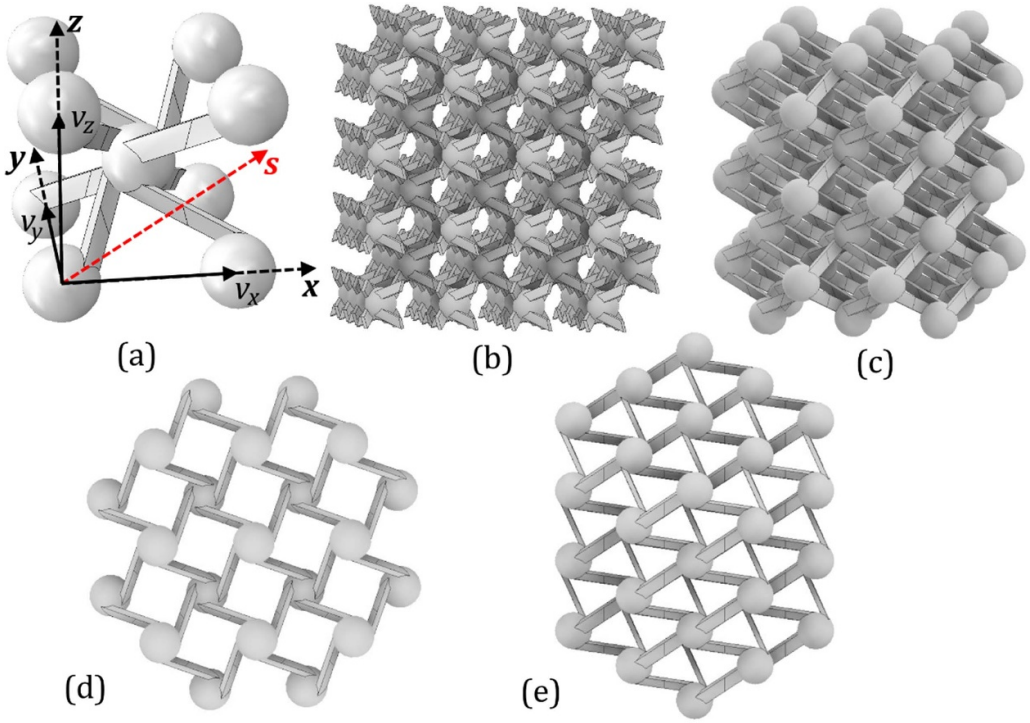

Figure 5. (a) BCC cell with axis *x, y, z, s*, and vectors v_x, v_y, v_z (b) complete structure, (c) the structure without all the spheres with less than four ligaments, (d) top view of the structure, (e) view from the [1,1,1] direction.

Table 1. Geometrical parameters of the MJF 3D printed structure.

r mm	*t* mm	*D* mm	*t/D* ratio mm	*r/D* ratio mm
5.35	0.8	22.5	0.15	0.238

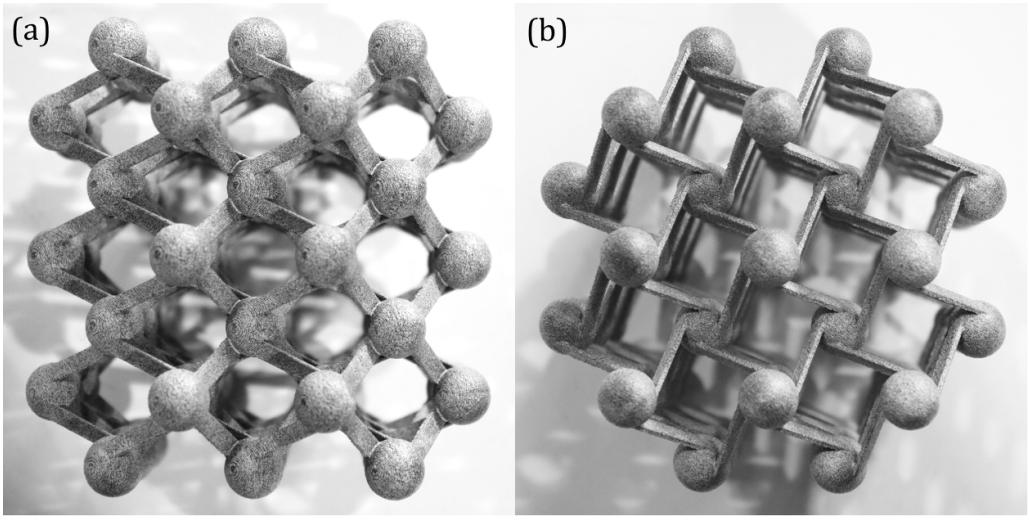

Figure 6. 3D printed structure (a) from the top view and (b) from the lateral view.

Table 2. List and details of the quasi-static compressive tests.

Test ID	Photo	Compression direction	Measurement face normal axis	Imposed displacement
Test 1	Figure 7(a)	*z*	*x*	5 *mm*
Test 2	Figure 7(a)	*z*	*x*	5 *mm*
Test 3	Figure 7(b)	*x*	*z*	2 *mm*
Test 4	Figure 7(c)	*x*	*x*	2 *mm*
Test 5	Figure 7(d)	*s*	*z*	2 *mm*

to maximize the contrast. A high-definition camera was set up to shoot a photo every 5 s. The resulting photos have a definition of $\sim 20\,\mathrm{pixel\,mm^{-1}}$. The strains were computed using a custom Matlab® code which measure the displacement of the centroid of the white dots on the spheres. Five quasi-static compression tests were performed, varying the loading direction and the face of strain measurement. The list of the tests is reported in table 2.

The configurations of the different tests are shown in figure 7, at the beginning of the test ($t0$) and in the moment of maximum load ($t1$). The yellow lines indicate the couples of points used to measure the strains. Normal/shear coupling was observed in all those configurations in which both the load axis and the strain measurement axis belong to *xy* plane, thus normal to *z*-direction (Test 3 and 5). This behavior was already observed in 2D chiral topologies [75, 76] and was related to anisotropy and chirality [77]. As an example, it is visible in tetra-chiral structures, but not in tetra-achiral structures and tri- or hexa-chiral structures, which are 'more isotropic' than tetra ones.

Let us now assume PR notation, such that:

$$\upsilon_{xy} = -\frac{\varepsilon_y}{\varepsilon_x}. \tag{4}$$

And let us remember that for the square symmetry defined before: $\upsilon_{xy} = \upsilon_{yx}$ and $\upsilon_{zx} = \upsilon_{zy}$. The results of the tests in terms of stiffness and PR are presented in table 3, while load/displacement curve and PR curve and shown in figure 8.

When loaded in different directions, the structure showed an initial linear response, followed by a deviation from linearity that causes a smooth and progressive reduction of stiffness. It could be addressed to the double contribution of the geometry and of the material behavior. When unloaded, the structure showed a certain amount of residual deformation, as shown in figure 8(a). Nonetheless, those deformations were fully recovered with time; thus, they must be addressed to the viscous behavior of the material.

All the tests show a very similar stiffness, except for Test 5. This is reasonable Test 5 was the only test in which the ligaments are more aligned to the load direction as shown in figure 8(a), thus offering a stiffer response. Tests 1 and 2 were performed in the same configuration and the force response is the same, even if in the second load the measured PR showed to be 20% more negative. This could be related to material settlements during the first loading, even if during the tests no damage or permanent deformation was observed. In Test 3 and 4, the load was applied in the same direction, thus they showed the same force response. In the first case, in which *PR* was measured along *z*-direction, the structure showed a distinct auxetic behavior, while in the second one, in which PR was measured along *y*-direction it results to be largely positive. Lastly, in Test 5 the structure shown an auxetic behavior

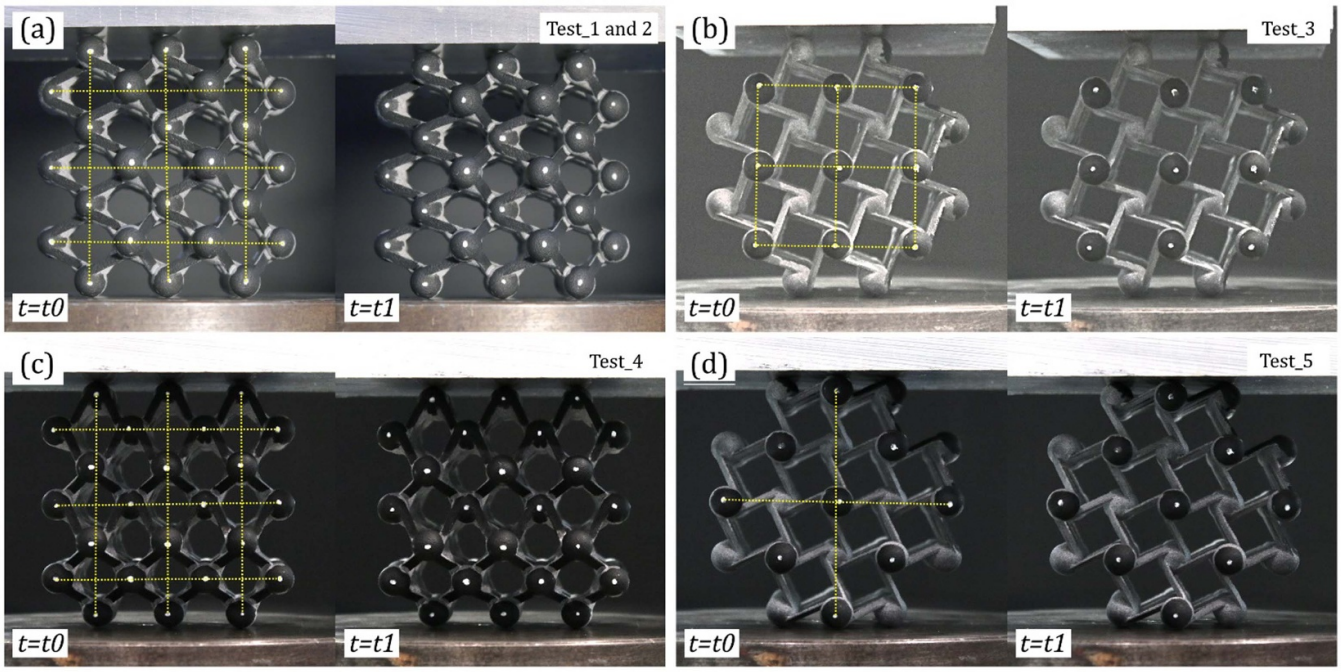

Figure 7. Different configurations of the quasi-static compression test, at the beginning and in the moment of maximum load. White dots and yellow lines can be noted.

Table 3. Stiffness and Poisson's ratio measured in each test. PR was measured in the point of maximum imposed compressive strain.

Test	Stiffness N mm^{-1}	PR —	Max imposed compressive strain
Test_1	$E_{zz} = 28$	$\upsilon_{zx} = -0.21$	6.9%
Test_2	$E_{zz} = 29.5$	$\upsilon_{zx} = -0.27$	7.2%
Test_3	$E_{xx} = 28$	$\upsilon_{xy} = 0.6$	2.3%
Test_4	$E_{xx} = 28.5$	$\upsilon_{xz} = -0.16$	2.5%
Test_5	$E_{ss} = 95$	$\upsilon_{ss} = 0$	3.4%

while loaded but not when unloaded, approaching to a PR $= 0$ with increasing imposed deformation. Concluding the tested geometry showed an appreciable auxetic behavior except for υ_{xy} and υ_{ss}, that are the two cases in which both the load axis and the PR measurement axis belongs to xy plane, normal to the sphere's rotation axis, z.

4. Numerical modeling

4.1. Modeling of compression tests

A FE numerical model was developed by using the Simulia/Abaqus environment and solved with Abaqus/Implicit solver, adopting finite strain theory. The aim is replicating the results of the compression tests to have an estimation of stress and strain field inside the structure, as well as of the sphere's rotation. The geometry was meshed with ten-nodes tetrahedral elements C3D10H, using a non-standard interior element growth algorithm to reduce the number of elements, by increasing the dimensions of the ones far from the outer surfaces, such as inside the spheres, as shown in figure 9(a). The complete mesh is composed of 421 426 elements with an average dimension of 0.5 mm, and 725 333 nodes. The result of a mesh size convergence study is reported in figure A1. A picture of the complete mesh in figure 9(b). Two equal forces were applied to the top and bottom rows of spheres, in the points where the structure was in contact with the machine during the experimental tests. Then, a set of isostatic constraints was defined to avoid rigid motions of the structure.

To have a basic characterization of the material, ten tensile specimens was 3D-printed with the same material and technique used to print the BCC structure. The adopted shape was suggested by ASTM D638 [78]. To have a simple check of the isotropy of the 3D-printed material, five specimens, labeled with the letter h, were printed with the longitudinal axis normal to the building direction, while the other five, labeled with the letter v, with longitudinal axis parallel to the building direction. The selected geometry with their orientation is shown in figure 10. They were equipped with an extensometer and tested with an imposed velocity of 0.5mm min^{-1}, using the same testing machine used for compression test of the chiral structure. The stress/strain curves are reported in figure 10. The material response is characterized by an initial linear region followed by a softening region. It shows a certain anisotropy, especially in the onset of nonlinearity and in the strain at failure. Nonetheless the initial slope seems to be not severely dependent on the printing orientation and the average Young's modulus, measured as the slope of the linear part of each curve, is 1.66 ± 0.16 GPa.

To represent the nonlinear behavior of Nylon 12 in the FE model a hyperelastic law was used with a strain energy potential in the form of a second order polynomial [79]:

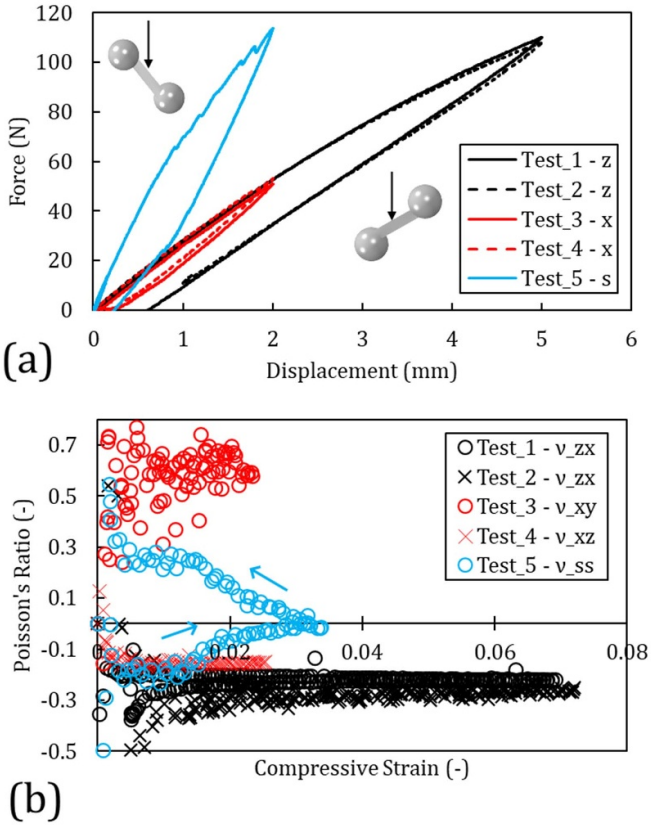

Figure 8. Results of the compression tests: (a) load/displacement response depending on the orientation of the ligaments, (b) Poisson's ratio measurements.

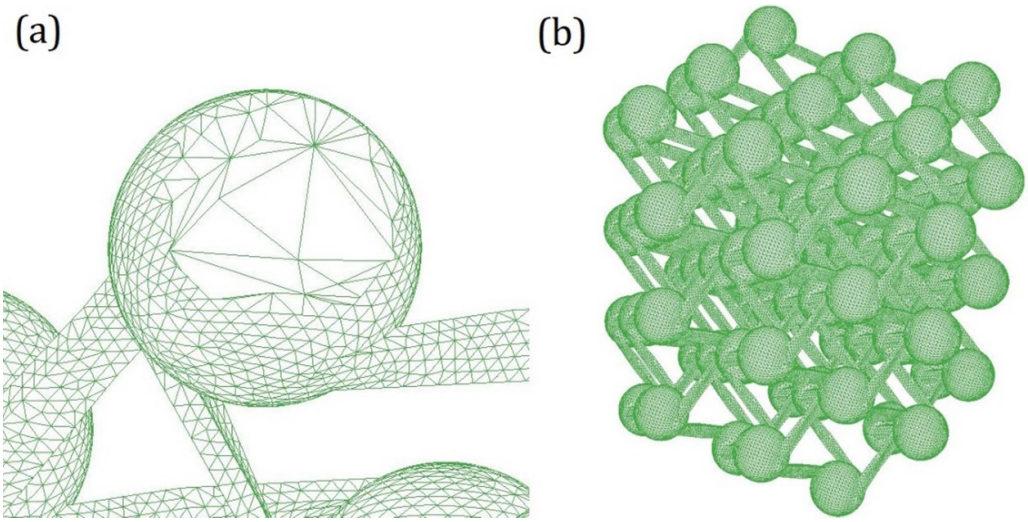

Figure 9. (a) View on the mesh pattern inside of a sphere, optimized a non-standard interior element growth algorithm and (b) complete mesh of the chiral structure.

$$U = C_{10}\cdot(\overline{I_1}-3)+C_{01}\cdot(\overline{I_2}-3)+C_{20}\cdot(\overline{I_1}-3)^2 + C_{11}\cdot(\overline{I_1}-3)\cdot(\overline{I_2}-3)+C_{02}\cdot(\overline{I_2}-3)^2. \quad (5)$$

In which $\overline{I_1}$ and $\overline{I_2}$ are the first and second invariant of the deviatoric strain tensor. By performing the partial derivative with respect to the strain tensor, the stress tensor is obtained. Considering that the second invariants are quadratic functions of the strain and that in this formulation they are raised to power higher than one, the obtained stress tensor will not be a linear function of the strain. Using the set of constants shown in table 4, the numerical curve shown in figure 10 was obtained.

With this model, all the compressive tests were reproduced to capture the force response and the PR. The comparison between the experimental and numerical curves is shown in

Table 4. Hyperelastic constants tuned to reproduce the Nylon 12 tensile behavior.

C_{10}	−5926.79
C_{01}	6297.46
C_{20}	−128 778
C_{11}	261 843
C_{02}	−126 627

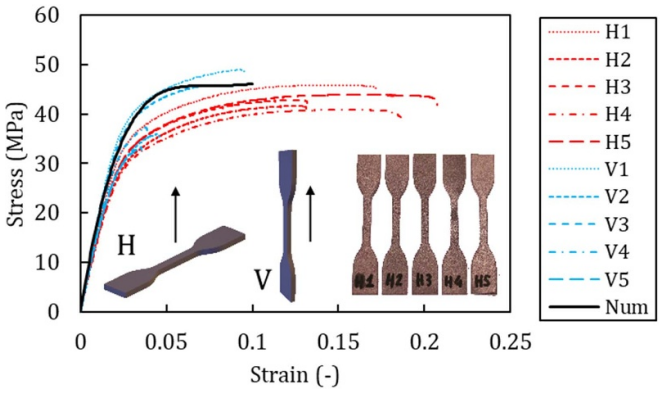

Figure 10. Stress/strain tensile response of MJF Nylon 12 specimens, used to characterize the material used to print the chiral structure. A detail of the printing orientation (H and V) of the specimens is shown.

figure 11, in term of (a) force response and (b) PR, for both which a good correlation was obtained. This correlated model allowed the determination of the angle of rotation of the spheres along their favored rotation axis, during the compression. Test 1 and 2, the ones which showed the more negative PR, have the higher rotation angle.

This first experimental and numerical investigation validated the concept of this structure, showing that imposing a favored rotation axis to the spheres, an appreciable auxetic behavior can be observed. The dependance of this auxetic behavior on the geometrical parameters of the structure must now be investigated.

4.2. Representative units and PBCs

If the experimental tests performed allow partial characterization of the structure, they were probably highly influenced by the edge effects. Thus, to obtain properties which are independent from those effects, numerical characterization was performed on a representative volume of the structure with PBCs applied. The effect of different values of *r/D* and *t/D* ratio on the different PRs was investigated.

Considering that the previous simulations show that most of the deformation developed in the ligaments, the spheres can be reasonably considered as rigid, thus simplifying the definitions of PBCs. In this way, the kinematics of the spheres can be fully described by the motion of a reference point (RP) in their center. As a representative volume, a BCC cell was chosen which for its symmetries guaranteed the correspondence of the RPs of edge spheres on opposite faces. The unit cell of a BCC lattice is made of one sphere (or atom) in the center of the cube and eight eighths of the sphere in the eight vertexes of the cube, but in the present case in which the spheres are rigid there is no need to take just eighths of the edge spheres. Thus, the representative volume used to model all the different configurations corresponds to a BCC cell, like the one shown in figure 5(a).

Applying PBCs to porous materials and meta-materials is not trivial. Some methods were already presented in [80], where PBC for normal loads were used, considering the possible internal rotations, in [81], where standard PBC were applied to two-dimensional metamaterials exploiting their symmetries, and in [82], where shape functions were defined at the edges of the representative volume to interpolate the displacement of non-corresponding mesh nodes into points with correspondence on the opposite face.

In this case, exploiting the assumption of rigidity of the sphere, a simplified technique was used. In fact, all the boundary conditions were applied only on the eight RPs of the eight external spheres, thus greatly simplifying their implementation. The 'dummy nodes' technique, described in [83], was used, in which a dummy node, unconnected from all the other nodes of the model and not belonging to any element, is introduced.

Being m and n any couple of RPs in corresponding position onto opposite faces of the representative volume with an initial distance L_0 between them, and u_j the translational degree of freedom parallel to the axis joining m and n, it must hold that:

$$u_j^n - u_j^m + u_j^{\text{dummy}} = 0. \tag{6}$$

So that, the relative displacement of each couple of m and n nodes is the same minus a constant, u_j^{dummy}, which is the displacement of the dummy node and $\frac{u_j^{\text{dummy}}}{L_0}$ is the magnitude of the imposed deformation along the axis joining m and n. Considering the assumption of rigidity of the spheres, equation (6) must be applied only to the eight RPs of the external spheres, for a total of twelve equations: four couples of RPs by three translational degrees of freedom.

But, for the same assumption, since the motion of the entire sphere is controlled by the motion of its RP, the rotational degrees of freedom of the RPs must be considered too. To guarantee compatibility, each couple of opposite RPs must have the same set of three rotation angles, around *x, y*, and *z*-axis; It is easy to show that in an eight RPs system, all the RPs must have the same three rotation angles. To do that, three further equations were introduced to impose that the three rotations of the eight RPs are equal to the three rotations of the dummy node:

$$u_k^{\text{RPs}} - u_k^{\text{dummy}} = 0 \tag{7}$$

where u_k represent the three rotational degrees of freedom. It must be noted that with this formulation, only a uniform stress state can be introduced in the structure. In the appendix, in

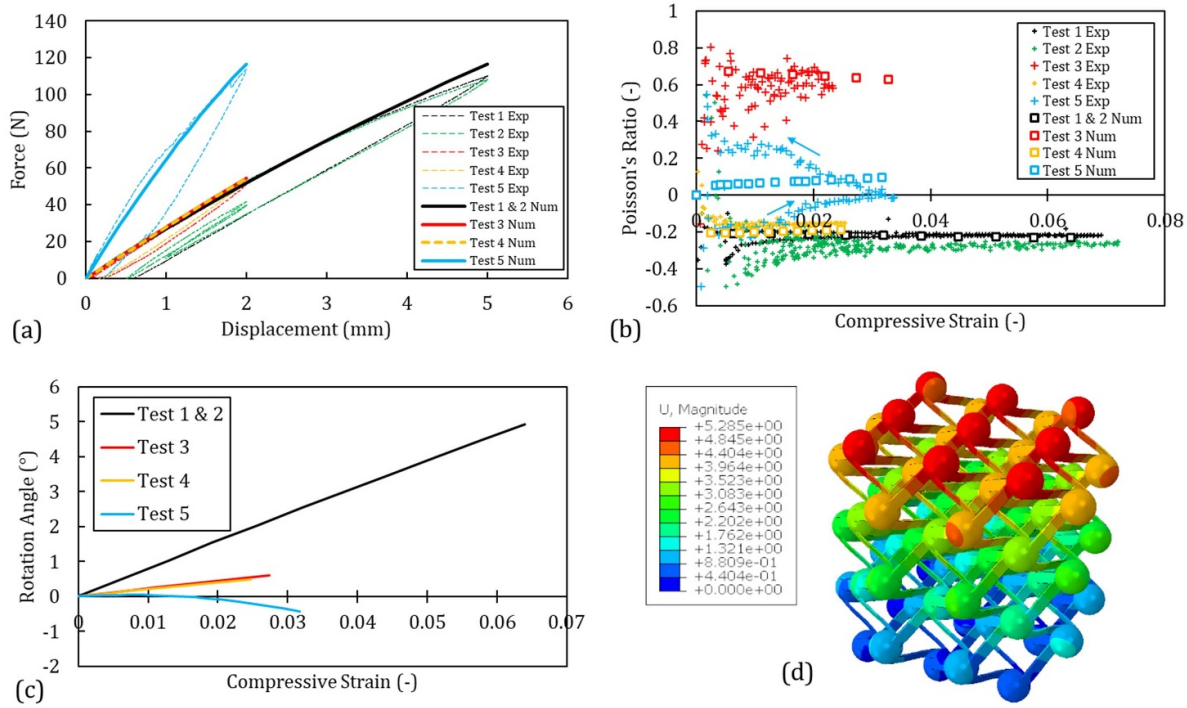

Figure 11. Numerical modeling of compression tests of the chiral structure: (a) experimental/numerical correlation of force and (b) Poisson's ratio. (c) Spheres rotation angle numerically determined; Positive angle refers to the rotation oriented as favored by the chiral disposition of the ligaments. (d) Displacement contour of Test 1 simulation.

figure A2(a) and (b) it is shown how using this method on the representative volume, the central sphere have the same rotation angles and half of the displacements of the edge spheres, thus no edge effect can be observed. Moreover, in figure A2(c), the comparison of the PR curves obtained with the representative volume and with a bigger structure, with three spheres per side, for a total of thirty-one spheres, is presented. The same behavior is observed, further proving the effectiveness of the PBCs.

4.3. Numerical investigation on geometrical parameters

Models of nine representative units with different values of *r/D* and *t/D* ratios were set up, using the PBC formulation described above. A perfectly elastic material law was used with $E = 10$ GPa and $\upsilon = 0.3$, but elastic properties do not influence the static properties of the structure. Tensile and compressive behavior was investigated in the different direction. Abaqus/Implicit solver was used, adopting finite strain theory. A uniform deformation was applied on the structures by applying a displacement to the dummy node. A set of isostatic constraint was set up to avoid rigid motions. The list of the different configuration is reported in table 5. In figure 12, the nine configurations with different values of *r/D* and *t/D* ratio are shown, together with their deformation modes when loaded along the *z, s*, and *x*-axis.

Some conclusions can be made looking at the deformation modes: remembering the reference system shown in figure 5(a), the auxetic behavior depends on the ratio between the ligament deflections around *z*-axis and *s*-axis. When the first is dominant, such as in configuration V, the spheres rotate around the *z*-axis driven by the chiral disposition of the ligaments, getting closer to each other, thus showing an auxetic behavior. When the second is dominant, such as in configuration II, the displacement/rotation coupling is not favored and the spheres move away from each other, resulting in a positive PR. After this consideration, it could be concluded that the bending anisotropy of the ligament is one of the keys to the functioning of this structure. Short, thin, and wide ligaments favor the spheres rotation around *z*-axis, leading to auxeticity. Observing the deformation mode of the BCC cell loaded along *s* and *x*-axis, the already mentioned coupling between

Table 5. List of the eight configurations investigated with their geometrical parameters.

ID	*r/D*	*t/D*
I	0.5	0.05
II	0.25	0.05
III	0.375	0.05
IV	0.625	0.05
V	0.75	0.05
VI	0.5	0.025
VII	0.5	0.0375
VIII	0.5	0.0625
IX	0.5	0.075

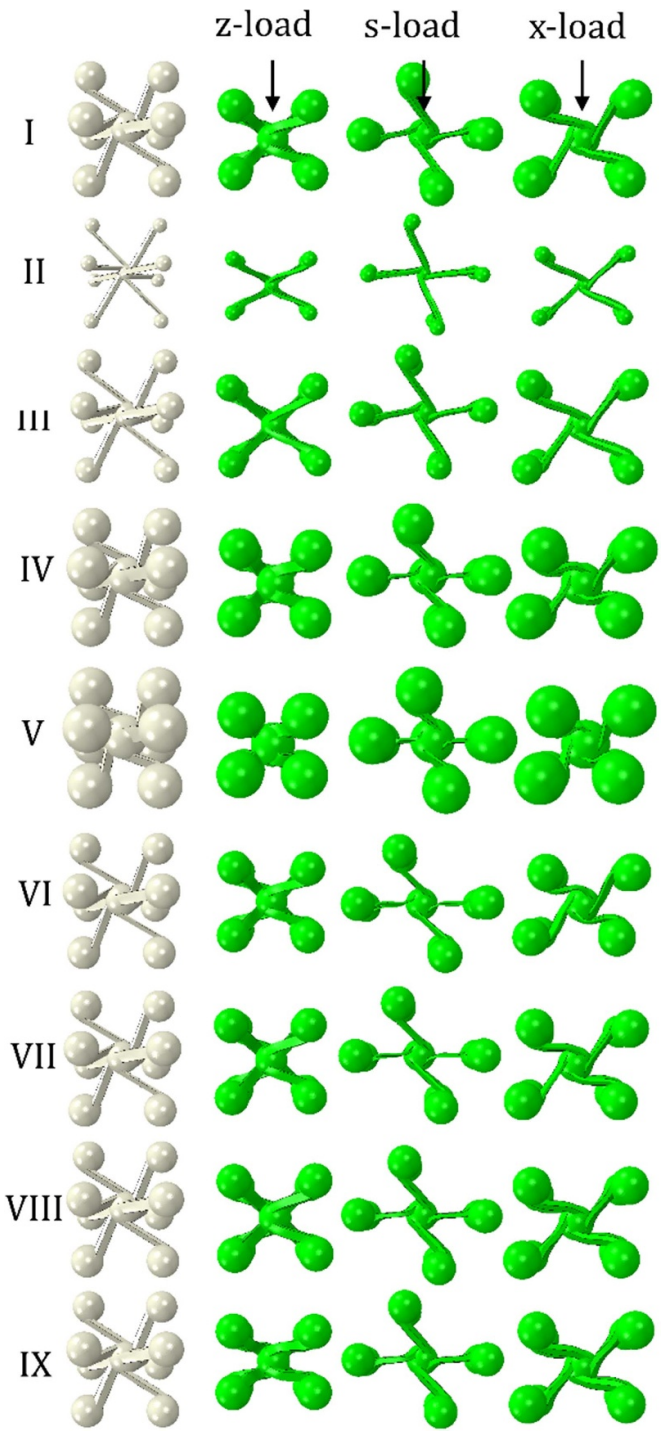

Figure 12. Representative units in different configurations with different *r/D* ratios.

axial and shear loads can be observed, more pronounced in the *s*-load case. Moreover, exceeding a certain threshold of tensile or compressive load, the structure becomes unstable. This instability will be investigated in the next paragraphs.

In figure 13, the force responses of the structure, loaded along *z, s*, and *x*-axis, are plotted, varying the *r/D* and *t/D* ratios. These curves show a quadratic relation between the force and displacement (as shown in red in figure 13(a)), with an increasing stiffness in tensile and a decreasing one in compression. By increasing the *r/D* and *t/D* ratios, thus by increasing the spheres radius and the ligaments thickness, an increasing stiffness is observed. If the ligament thickness contribution to the stiffness is direct, the link between spheres radius and stiffness could be found considering that, larger spheres radius led to wider, thus stiffer, ligaments.

In figures 14(a) and (b), the relationships between the initial tensile and compressive stiffness of the structures and the two geometrical parameters, (a) *r/D* and (b) *t/D*, are shown. The initial stiffnesses were measured at small deformations and were used to be compared among the different configurations. As expected, they grew monotonically with both *r/D* and *t/D*, even if the tensile stiffness tends to be slightly higher than the compressive one. These relationships were fit with quadratic polynomials and the coefficients of determination were never below 0.96. Examples of quadratic fit are reported in figure. In the first case, this growth is more pronounced along the *z*-axis, because a load in that direction directly insists on the width of the ligaments which grows with spheres radius. In the second case, the quadratic relationship suggests that global stiffness is not dominated by the ligaments bending stiffness, although it would be expected to be cubic. Its influence could be probably reduced by the torsional compliance of the spheres. In figures 14(c) and (d), the relationships between the tensile and compressive instability load of the structures and the two geometrical parameters, (c) *r/D* and (d) *t/D*, are shown. Again, the instability loads increase with increasing *r/D* and *t/D*. This relationship could be fitted with a quadratic polynomial with a coefficient of determination higher than 0.97.

In figure 14(e), an exemplificative case of the rotations around *x, y*, and *z*-axis (following the reference system shown in figure 5(a)) of two spheres, the central one and one belonging to the edge, is shown. In a large range of displacement, only *z*-rotation is present, which is the favored by the ligament chiral pattern. Central and edge spheres rotate at the same angles: this is a sign of the good quality of PBC, since any edge effect affects the spheres rotations. Going outside the central range of displacement, the secondary rotations (*x* and *y* ones) angles became different from zero. It is interesting to notice that these secondary rotations typically appear in correspondence to the onset of instability, as shown in figure 14(f), even if this effect is more pronounced in case of compressive instability.

Lastly, in figure 15 two PRs measured in two directions normal to the loading direction (still in the reference system presented in figure 5(a)) as a function of the two geometrical parameters, *r/D* and *t/D*, are plotted, for all the configurations reported in table 5, loaded along (a and b) *z*, (c and d) *s*, and (e and f) *x*-axis. The different PRs were computed as in equation (4), measuring the strain as the distance of two spheres, along the measuring direction. The general trend shows that the structure exhibits a more pronounced auxetic behavior for larger sphere's radius and thinner ligaments, with the PR linearly increasing with an applied tensile strain and decreasing with a compressive one, as long as the structure remains stable.

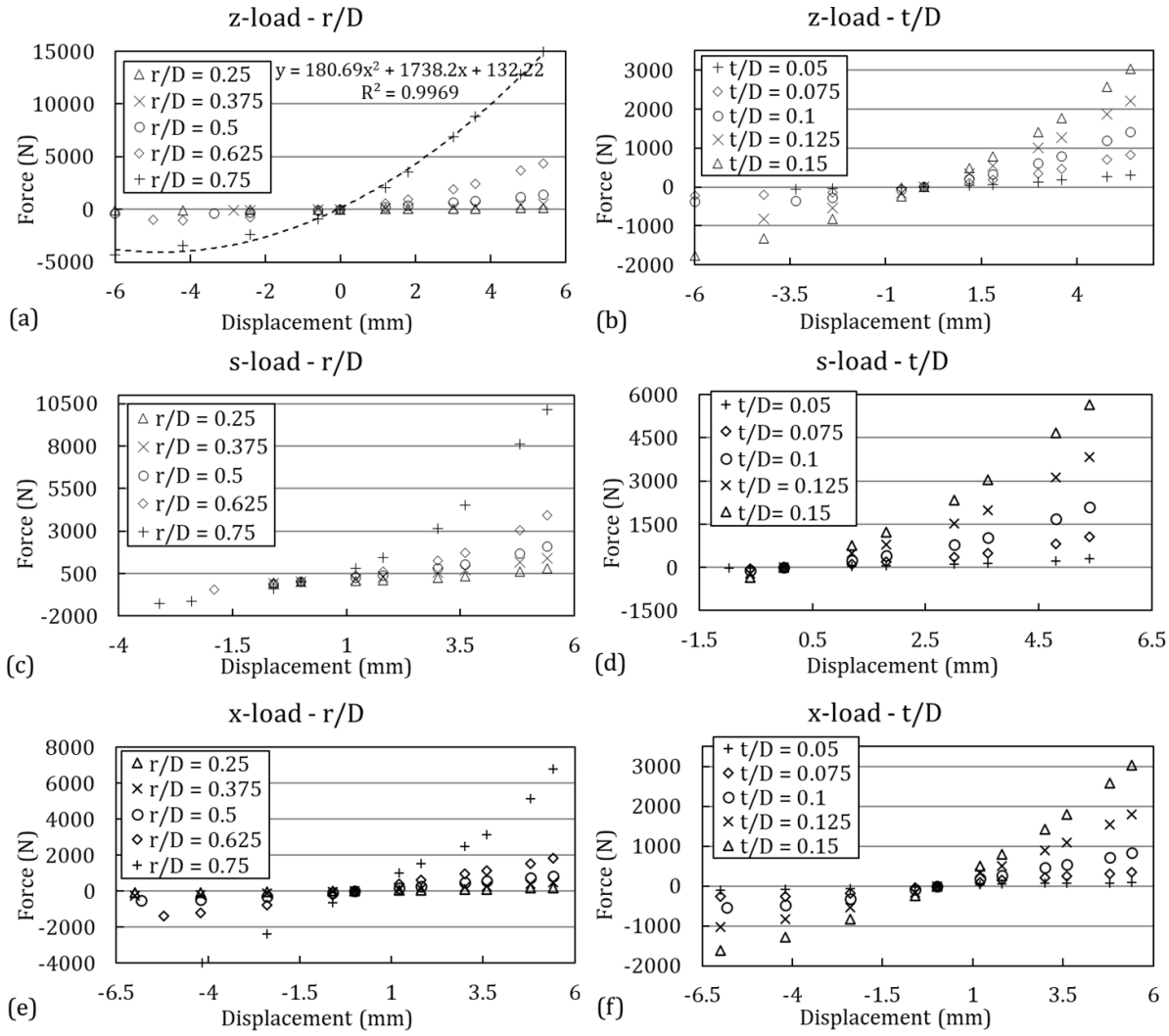

Figure 13. Force/displacement curves of the different configurations of BCC representative unit: (a) *r/D* and (b) *t/D* ratio influence when the structure is loaded along *z*-axis, (c) and (d) *s*-axis, and (e) and (f) *x*-axis.

With the right combination of the values of the two geometrical parameters, an auxetic behavior can be obtained in every load direction, in some cases simultaneously (see the case $r/D = 0.75$). A first aspect to be noted is that in the z-load case, the PR shows a transversally isotropic behavior, thus the same PR can be measured in any axis belonging to the plane normal to the *z*-axis [84, 85]. On the other hand, in the *s*-load case, PR lower than -1, and even -2 (see $t/r = 0.15$), can be obtained after the onset of the compressive instability, with a sudden variation of trend typical of the snap-through effect.

The value which PRs can assume is related to the stability of the material or meta-material. For an stable isotropic material, it holds that $\upsilon \in (-1,\ 0.5)$ [84, 85]; it must be noted that this interval is open: in fact, a PR $= -1$ would lead to an indeterminacy ($G \to \infty$) [37]. In the case of orthotropic or anisotropic materials there are not hard boundaries on the value of PRs given by stability conditions. In the specific subcase of transversal isotropy, the stability range of PRs become $(-1,\ 1)$. It can be noted that in the *z*-load cases, in which the structure showed transversal isotropy, this rule is respected (see figures 15(a) and (b)). Even if for anisotropic systems it is not forbidden by stability considerations, the appearance of a PR lower than -1 remains a peculiar phenomenon, Examples of PR reaching values lower -1 were observed in [86, 87], in the second case, reaching the exceptional value of -13. In both these works, this effect was addressed to the strong anisotropy of the meta-material. It is interesting that, in the present work, the threshold of -1 was negatively exceeded in the presence of structural instability. After the snap-through, structures typically experience a change of stiffness, thus it can be reasonably supposed that this change of stiffness could lead to an increased anisotropy which could cause the exceptional values of PR.

5. Conclusions

This work presents a novel three-dimensional BCC chiral geometry, which can exhibit negative PRs, depending on its geometrical parameters. This geometry is made of spheres placed

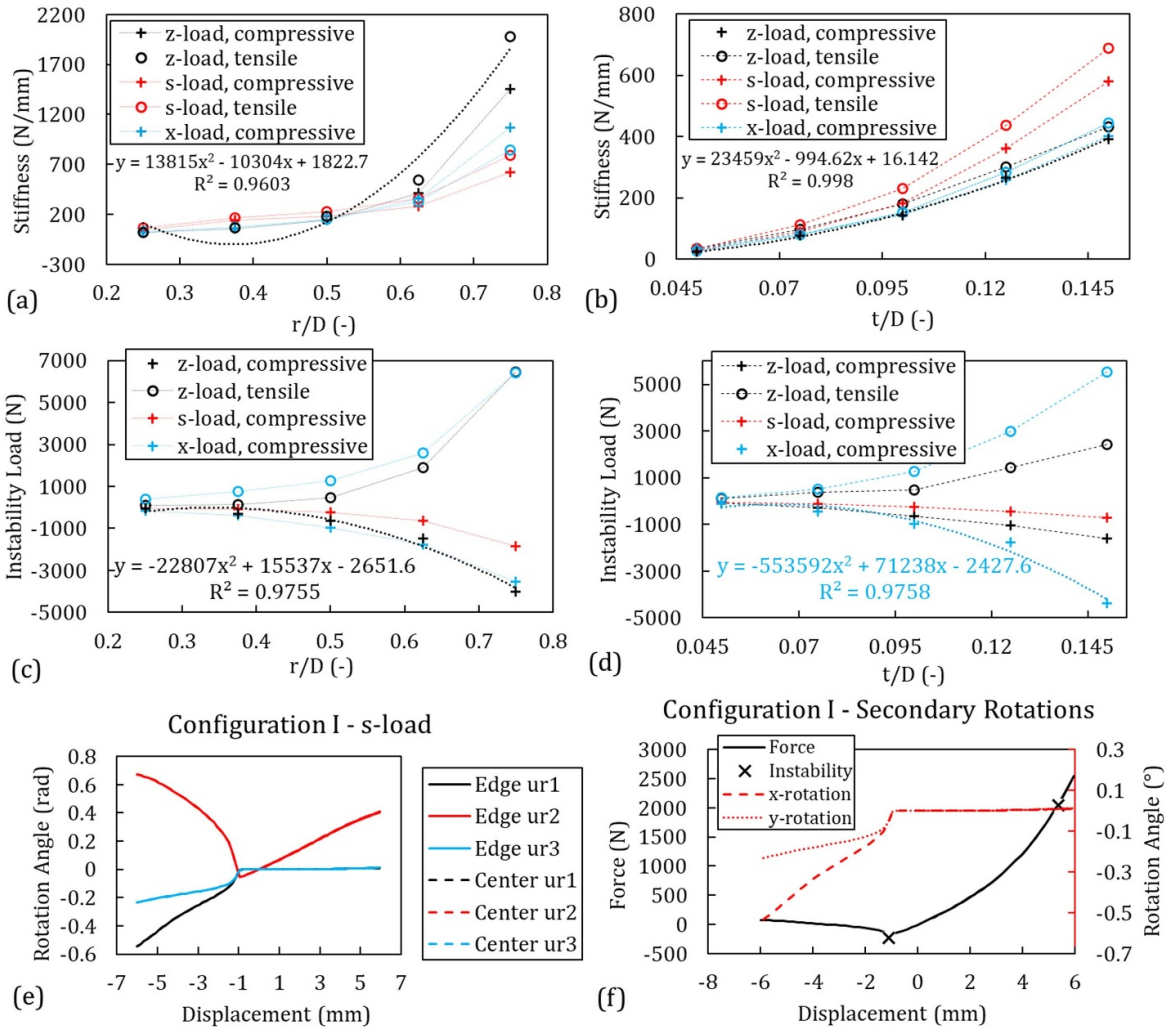

Figure 14. Dependance of compressive and tensile (a and b) initial stiffness and (c and d) instability load on *r/D* and *t/D* ratios, along *z, s*, and *x*-axis. (f) Correlation between instability loads and secondary rotations.

in the three-dimensional space following a BCC periodicity. Each sphere is connected to its closest neighbors by eight ligaments. Its working principle relies on the induction of a coupling of the displacement and rotation of the spheres and on the definition of a favored rotation axis. A sample of this geometry was 3D-printed and mechanically tested, showing a negative PR, up to -0.27, as a response to the compression in certain directions. A FE model to reproduce the experimental tests was developed and validated by correctly reproducing the force and PR response of the 3D-printed structure. Then, a numerical investigation on the influence of geometrical parameters on the stiffness, PR, and instability load, was performed on small representative units coupled with a set of PBCs. This investigation shows that the structure has a quadratic force/displacement response, as well as that thicker ligaments and bigger sphere lead to an increased stiffness and to an increased instability load, thus more stable structures, both in tension and compression. All these relationships behave following a quadratic trend; thus, the deformation of the structure is not dominated by the ligaments bending only. On the other hand, thinner ligaments and bigger spheres lead to more pronounced auxetic behavior. With the right combination of geometrical parameters, the BCC structure exhibits a negative PR approaching the value of -1, regardless of the loading direction. Moreover, in the plane normal to the favored rotation axis, normal/shear coupling was observed, as well as a transversally isotropic behavior of the PR. Lastly, from this work some more general considerations can be made about the auxetic behavior, the chirality, and the instability of sphere-based structures:

- In previous literature works, fully chiral 3D structures were developed. In those configurations, sphere can have infinite possible rotation axes, thus leading to intrinsically unstable structures, with PR that hardly goes below zero. Thus, the imposition of a favored rotation axis, i.e. the stabilization of the structure, unlocks the auxetic behavior of sphere-based

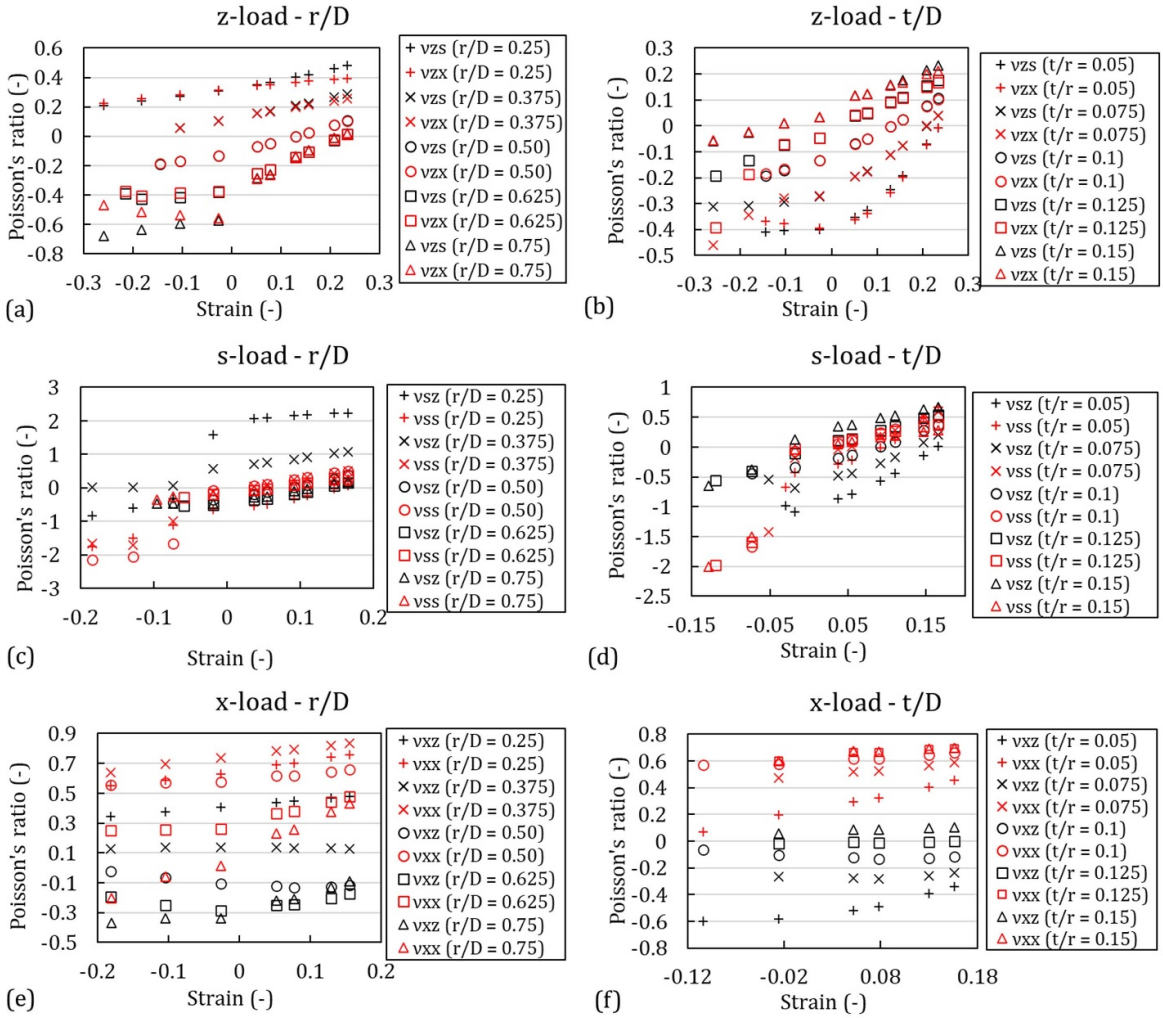

Figure 15. Poisson's ratio curves of the different configurations of BCC representative unit: (a) *r/D* and (b) *t/D* ratio influence when the structure is loaded along *z*-axis, (c) and (d) *s*-axis, and (e) and (f) *x*-axis.

structures. Indeed, in the structure presented in this work, secondary rotations and the onset of instability are closely linked, typically happening simultaneously.

- The auxetic behavior of chiral sphere-based structures is determined by the competition of two bending modes of the ligament, around different axes. When the ligaments bend around the sphere's favored rotation axis, they tend to wrap around the spheres themselves, thus favoring the displacement/rotation coupling which lead to a negative PR. When ligaments bend around other axes, the spheres tend to move away leading to a positive PR. It can be concluded that optimal ligaments must have an anisotropic bending stiffness, i.e. large width and small thickness, assuming a ribbon shape.
- The working principle of this structure could be extended to many different periodic dispositions of spheres in the three-dimensional space.

Data availability statement

All data that support the findings of this study are included within the article (and any supplementary files).

Funding statement

This research received no specific grant from any funding agency in the public, commercial, or not-for-profit sectors.

Appendix

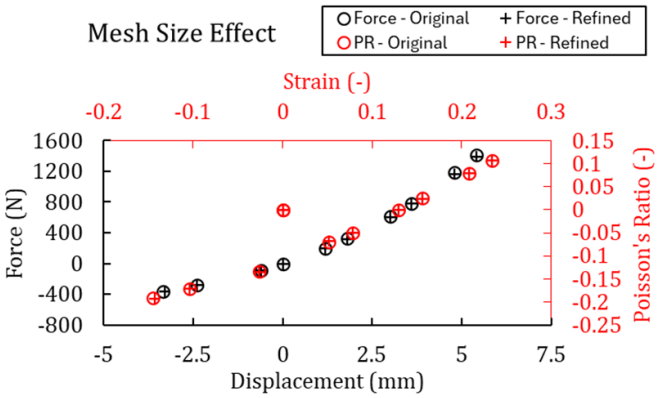

Figure A1. Comparison of force vs. displacement and Poisson's ratio vs applied strain of a representative volume with PBC (as explained in Section XX) using different meshes: The first with elements with average dimension of 0.5 mm (the same used in all the analyses) and second with elements with average dimension of 0.25 mm.

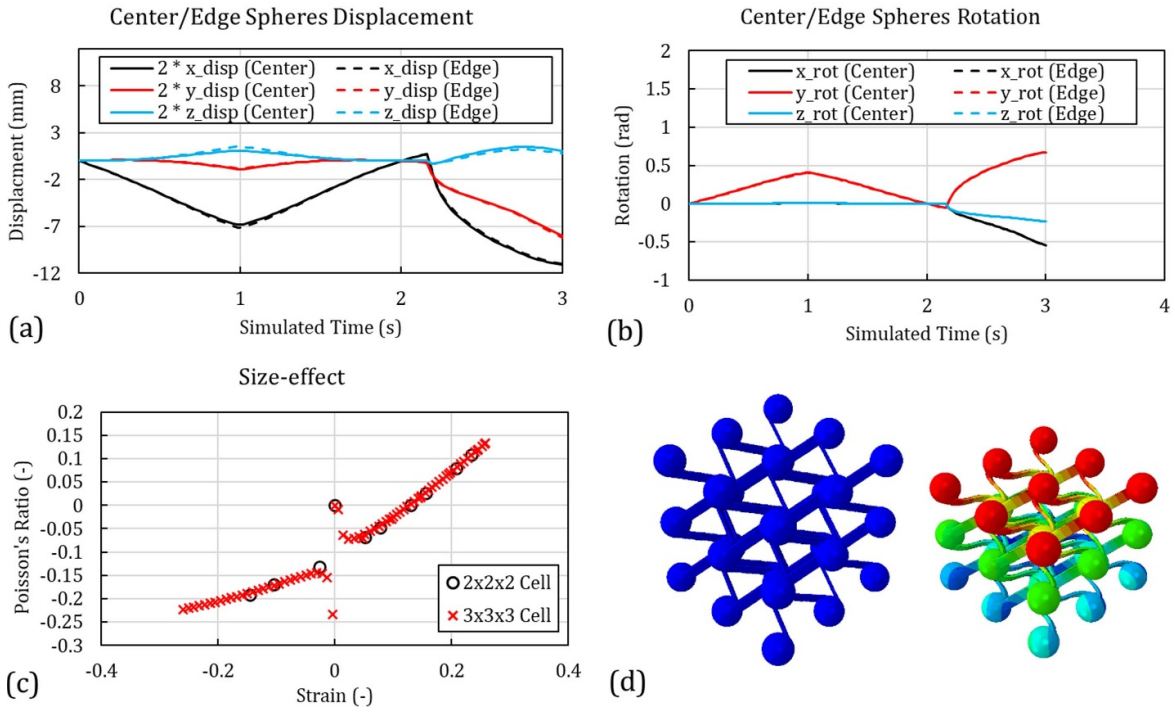

Figure A2. Comparison between (a) the displacements and (b) the rotation angles of the central sphere and one edge spheres. (c) Comparison between the PR curves obtained with the representative volume ($2 \times 2 \times 2$ spheres) and a bigger one ($3 \times 3 \times 3$), shown in (d).

ORCID iDs

Antonio Maria Caporale https://orcid.org/0000-0001-8094-6717
Alessandro Airoldi https://orcid.org/0000-0002-4938-3407
Nejc Novak https://orcid.org/0000-0001-8263-9753

References

[1] Gibson L J and Ashby M F 1997 *Cellular Solids: Structure and Properties* 2nd edn (Cambridge University Press)
[2] Wu W, Hu W, Qian G, Liao H, Xu X and Berto F 2019 Mechanical design and multifunctional applications of chiral mechanical metamaterials: a review *Mater. Des.* **180** 107950
[3] Novak N, Vesenjak M and Ren Z 2017 Computational simulation and optimization of functionally graded auxetic structures made from inverted tetrapods *Phys. Status Solidi* b **254** 1600753
[4] Lakes R 1987 Foam structures with a negative Poisson's ratio *Science* **235** 1038–40
[5] Wojciechowski K W 1987 Constant thermodynamic tension Monte Carlo studies of elastic properties of a two-dimensional system of hard cyclic hexamers *Mol. Phys.* **61** 1247–58
[6] Smith C W, Grima J N and Evans K E 2000 A novel mechanism for generating auxetic behaviour in reticulated foams: missing rib foam model *Acta Mater.* **48** 4349–56
[7] Wojciechowski K W 2003 Non-chiral, molecular model of negative Poisson ratio in two dimensions *J. Phys. A: Math. Gen.* **36** 11765–78
[8] Ren X, Das R, Tran P, Ngo T D and Xie Y M 2018 Auxetic metamaterials and structures: a review *Smart Mater. Struct.* **27** 023001
[9] Caddock B D and Evans K E 1989 Microporous materials with negative Poisson's ratios. I. microstructure and mechanical properties *J. Phys. D: Appl. Phys.* **22** 1877–82
[10] Evans K E and Caddock B D 1989 Microporous materials with negative Poisson's ratios. II. Mechanisms and interpretation *J. Phys. D: Appl. Phys.* **22** 1883–7
[11] Goldstein R V, Gorodtsov V A and Lisovenko D S 2010 Auxetic mechanics of crystalline materials *Mech. Solids* **45** 529–45
[12] Yao Y T, Uzun M and Patel I 2011 Workings of auxetic nano-materials *J. Achieve. Mater. Manuf. Eng.* **49** 585–93
[13] Schwerdtfeger J, Heinl P, Singer R F and Körner C 2010 Auxetic cellular structures through selective electron-beam melting *Phys. Status Solidi* b **247** 269–72
[14] Grima J N and Evans K E 2000 Auxetic behavior from rotating squares *J. Mater. Sci. Lett.* **19** 1563–5
[15] Grima J N, Alderson A and Evans K E 2005 Auxetic behaviour from rotating rigid units *Phys. Status Solidi* b **242** 561–75
[16] Lakes R 1991 Deformation mechanisms in negative Poisson's ratio materials: structural aspects *J. Mater. Sci.* **26** 2287–92
[17] Bilski M, Wojciechowski K W, Stręk T, Kędziora P, Grima-Cornish J N and Dudek M R 2021 Extremely non-auxetic behavior of a typical auxetic microstructure due to its material properties *Materials* **14** 7837
[18] Bilski M, Pigłowski P M and Wojciechowski K W 2021 Extreme Poisson's ratios of honeycomb, Re-entrant, and zig-zag crystals of binary hard discs *Symmetry* **13** 1127
[19] Pozniak A A and Wojciechowski K W 2014 Poisson's ratio of rectangular anti-chiral structures with size dispersion of circular nodes: Poisson's ratio of rectangular anti-chiral structures *Phys. Status Solidi* b **251** 367–74
[20] Mizzi L, Attard D, Gatt R, Pozniak A A, Wojciechowski K W and Grima J N 2015 Influence of translational disorder on the mechanical properties of hexachiral honeycomb systems *Composites* B **80** 84–91
[21] Novak N, Vesenjak M and Ren Z 2016 Auxetic cellular materials—a review *SV-JME* **62** 485–93
[22] Yang W, Li Z-M, Shi W, Xie B-H and Yang M-B 2004 Review on auxetic materials *J. Mater. Sci.* **39** 3269–79
[23] Scarpa F, Ciffo L G and Yates J R 2004 Dynamic properties of high structural integrity auxetic open cell foam *Smart Mater. Struct.* **13** 49–56
[24] Krödel S, Delpero T, Bergamini A, Ermanni P and Kochmann D M 2014 3 D auxetic microlattices with independently controllable acoustic band gaps and quasi-s tatic elastic moduli *Adv. Eng. Mater.* **16** 357–63
[25] Yang S, Qi C, Wang D, Gao R, Hu H and Shu J 2013 A comparative study of ballistic resistance of sandwich panels with aluminum foam and auxetic honeycomb cores *Adv. Mech. Eng.* **5** 589216
[26] Chan N and Evans K E 1998 Indentation resilience of conventional and auxetic foams *J. Cell Plast* **34** 231–60
[27] Novak N, Starčevič L, Vesenjak M and Ren Z 2019 Blast response study of the sandwich composite panels with 3D chiral auxetic core *Compos. Struct.* **210** 167–78
[28] Chen C, Airoldi A, Caporale A M, Sala G and Yin X 2024 Impact response of composite energy absorbers based on foam-filled metallic and polymeric auxetic frames *Compos. Struct.* **331** 117916
[29] Tomažinčič D, Vesenjak M and Klemenc J 2020 Prediction of static and low-cycle durability of porous cellular structures with positive and negative Poisson's ratios *Theor. Appl. Fract. Mech.* **106** 102479
[30] Nečemer B, Kramberger J, Vuherer T and Glodež S 2019 Fatigue crack initiation and propagation in re-entrant auxetic cellular structures *Int. J. Fatigue* **126** 241–7
[31] Kramberger J, Nečemer B and Glodež S 2019 Assessing the cracking behavior of auxetic cellular structures by using both a numerical and an experimental approach *Theor. Appl. Fract. Mech.* **101** 17–24
[32] Imbalzano G, Tran P, Ngo T D and Lee P V S 2016 A numerical study of auxetic composite panels under blast loadings *Compos. Struct.* **135** 339–52
[33] Imbalzano G, Tran P, Ngo T D and Lee P V 2017 Three-dimensional modelling of auxetic sandwich panels for localised impact resistance *J. Sandwich Struct. Mater.* **19** 291–316
[34] Al-Rifaie H, Novak N, Vesenjak M, Ren Z and Sumelka W 2022 Fabrication and mechanical testing of the uniaxial graded auxetic damper *Materials* **15** 387
[35] Novak N, Al-Rifaie H, Airoldi A, Krstulović-Opara L, Łodygowski T, Ren Z and Vesenjak M 2023 Quasi-static and impact behaviour of foam-filled graded auxetic panel *Int. J. Impact Eng.* **178** 104606
[36] Prall D and Lakes R S 1997 Properties of a chiral honeycomb with a Poisson's ratio of −1 *Int. J. Mech. Sci.* **39** 305–14
[37] Spadoni A and Ruzzene M 2012 Elasto-static micropolar behavior of a chiral auxetic lattice *J. Mech. Phys. Solids* **60** 156–71
[38] Alderson A, Alderson K L, Attard D, Evans K E, Gatt R, Grima J N, Miller W, Ravirala N, Smith C W and Zied K 2010 Elastic constants of 3-, 4- and 6-connected chiral and anti-chiral honeycombs subject to uniaxial in-plane loading *Compos. Sci. Technol.* **70** 1042–8
[39] Mizzi L and Spaggiari A 2021 Chiralisation of Euclidean polygonal tessellations for the design of new auxetic metamaterials *Mech. Mater.* **153** 103698
[40] Mizzi L and Spaggiari A 2022 Novel chiral honeycombs based on octahedral and dodecahedral Euclidean polygonal tessellations *Int. J. Solids Struct.* **238** 111428

[41] Mizzi L, Grasselli L, Spaggiari A, Gatt R, Farrugia P-S and Grima J N 2023 Design of isotropic 2D chiral metamaterials based on monohedral pentagonal tessellations *Thin-Walled Struct.* **187** 110739
[42] Mizzi L, Simonetti A and Spaggiari A 2024 Mechanical properties and failure modes of additively-manufactured chiral metamaterials based on Euclidean tessellations: an experimental and finite element study *RPJ* **30** 59–71
[43] Alderson A, Alderson K L, Chirima G, Ravirala N and Zied K M 2010 The in-plane linear elastic constants and out-of-plane bending of 3-coordinated ligament and cylinder-ligament honeycombs *Compos. Sci. Technol.* **70** 1034–41
[44] Chen Y J, Scarpa F, Liu Y J and Leng J S 2013 Elasticity of anti-tetrachiral anisotropic lattices *Int. J. Solids Struct.* **50** 996–1004
[45] Lorato A, Innocenti P, Scarpa F, Alderson A, Alderson K L, Zied K M, Ravirala N, Miller W, Smith C W and Evans K E 2010 The transverse elastic properties of chiral honeycombs *Compos. Sci. Technol.* **70** 1057–63
[46] Abramovitch H, Burgard M, Edery-Azulay L, Evans K E, Hoffmeister M, Miller W, Scarpa F, Smith C W and Tee K F 2010 Smart tetrachiral and hexachiral honeycomb: sensing and impact detection *Compos. Sci. Technol.* **70** 1072–9
[47] Airoldi A, Bettini P, Panichelli P, Oktem M F and Sala G 2015 Chiral topologies for composite morphing structures—Part I: development of a chiral rib for deformable airfoils *Phys. Status Solidi* b **252** 1435–45
[48] Airoldi A, Bettini P, Panichelli P and Sala G 2015 Chiral topologies for composite morphing structures—Part II: novel configurations and technological processes *Phys. Status Solidi* b **252** 1446–54
[49] Airoldi A, Novak N, Sgobba F, Gilardelli A and Borovinšek M 2020 Foam-filled energy absorbers with auxetic behaviour for localized impacts *Mater. Sci. Eng.* **788** 139500
[50] Spadoni A, Ruzzene M and Scarpa F 2005 Global and local linear buckling behavior of a chiral cellular structure *Phys. Status Solidi* b **242** 695–709
[51] Miller W, Smith C W, Scarpa F and Evans K E 2010 Flatwise buckling optimization of hexachiral and tetrachiral honeycombs *Compos. Sci. Technol.* **70** 1049–56
[52] Wang F 2018 Systematic design of 3D auxetic lattice materials with programmable Poisson's ratio for finite strains *J. Mech. Phys. Solids* **114** 303–18
[53] Mukhopadhyay T and Kundu D 2022 Mixed-mode multidirectional Poisson's ratio modulation in auxetic 3D lattice metamaterials *Adv. Eng. Mater.* **24** 2101183
[54] Shen J, Zeng Q, Wang J, Ge J, Gao F and Liang J 2023 Study of mechanical properties of a new 3D re-entrant lattice auxetic structure under bending *Adv. Eng. Mater.* **25** 2201509
[55] Novak N, Mauko A, Ulbin M, Krstulović-Opara L, Ren Z and Vesenjak M 2022 Development and characterisation of novel three-dimensional axisymmetric chiral auxetic structures *J. Mater. Res. Technol.* **17** 2701–13
[56] Mauko A, Emre Yilmaz Y, Novak N, Doktor T, Vesenjak M and Ren Z 2024 Dynamic characterisation of novel three-dimensional axisymmetric chiral auxetic structure *Compos. Struct.* **333** 117949
[57] Novak N, Nowak M, Vesenjak M and Ren Z 2022 Structural optimization of the novel 3D graded axisymmetric chiral auxetic structure *Phys. Status Solidi* b **259** 2200409
[58] Lim T 2016 A 3D auxetic material based on intersecting double arrowheads *Phys. Status Solidi* b **253** 1252–60
[59] Kim D-Y, Kim H-S, Kamath S S, Hou X, Choi J-W and Park S-H 2024 TPMS-based auxetic structure for high-performance airless tires with variable stiffness depending on deformation *Sci. Rep.* **14** 11419
[60] Liu B, Feng J, Lin Z, He Y and Fu J 2023 Controllable three-dimension auxetic structure design strategies based on triply periodic minimal surfaces and the application in hip implant *Virtual Phys. Prototype.* **18** e2170890
[61] Zhang W, Yin H, Wu Y, Jin Q, Wu L, Wen G, Liu J and Wu X 2023 A novel auxetic 3D lattice structure for enhancing energy absorption *Compos. Struct.* **326** 117620
[62] Cabras L and Brun M 2016 A class of auxetic three-dimensional lattices *J. Mech. Phys. Solids* **91** 56–72
[63] Galea R, Farrugia P-S, Dudek K K, Attard D, Grima J N and Gatt R 2023 A novel design method to produce 3D auxetic metamaterials with continuous pores exemplified through 3D rotating auxetic systems *Mater. Des.* **226** 111596
[64] Zong H, Zhang H, Wang Y, Wang M Y and Fuh J Y H 2018 On two-step design of microstructure with desired Poisson's ratio for AM *Mater. Des.* **159** 90–102
[65] Xia R, Song X, Sun L, Wu W, Li C, Cheng T and Qian G 2018 Mechanical properties of 3D isotropic anti-tetrachiral metastructure *Phys. Status Solidi* b **255** 1700343
[66] Wu W, Qi D, Liao H, Qian G, Geng L, Niu Y and Liang J 2018 Deformation mechanism of innovative 3D chiral metamaterials *Sci. Rep.* **8** 12575
[67] Ha C S, Plesha M E and Lakes R S 2016 Chiral three-dimensional isotropic lattices with negative Poisson's ratio *Phys. Status Solidi* b **253** 1243–51
[68] Duan S, Wen W and Fang D 2018 A predictive micropolar continuum model for a novel three-dimensional chiral lattice with size effect and tension-twist coupling behavior *J. Mech. Phys. Solids* **121** 23–46
[69] Li J, Ha C S and Lakes R S 2020 Observation of squeeze–twist coupling in a chiral 3D isotropic lattice *Phys. Status Solidi* B **257** 1900140
[70] Ren X, Shen J, Ghaedizadeh A, Tian H and Min Xie Y 2015 Experiments and parametric studies on 3D metallic auxetic metamaterials with tuneable mechanical properties *Smart Mater. Struct.* **24** 095016
[71] Ren X, Shen J, Tran P, Ngo T D and Xie Y M 2018 Design and characterisation of a tuneable 3D buckling-induced auxetic metamaterial *Mater. Des.* **139** 336–42
[72] Xu Z, Wang Y, Wu D, Ananth K P and Bai J 2019 The process and performance comparison of polyamide 12 manufactured by multi jet fusion and selective laser sintering *J. Manuf. Process.* **47** 419–26
[73] Cai C, Tey W S, Chen J, Zhu W, Liu X, Liu T, Zhao L and Zhou K 2021 Comparative study on 3D printing of polyamide 12 by selective laser sintering and multi jet fusion *J. Mater. Process. Technol.* **288** 116882
[74] Rosso S, Meneghello R, Biasetto L, Grigolato L, Concheri G and Savio G 2020 In-depth comparison of polyamide 12 parts manufactured by multi jet fusion and selective laser sintering *Addit. Manuf.* **36** 101713
[75] Zhou X, Liang X, Liu Z, Tao C and Li H 2022 Compression deformation prediction of chiral metamaterials: a compression–shear coupling model *Materials* **15** 5180
[76] Karathanasopoulos N, Dos Reis F, Diamantopoulou M and Ganghoffer J-F 2020 Mechanics of beams made from chiral metamaterials: tuning deflections through normal-shear strain couplings *Mater. Des.* **189** 108520
[77] Yuan Z, Cui Z and Ju J 2021 Micropolar homogenization of wavy tetra-chiral and tetra-achiral lattices to identify axial–shear coupling and directional negative Poisson's ratio *Mater. Des.* **201** 109483
[78] D20 Committee Test method for tensile properties of plastics (https://doi.org/10.1520/D0638-14)
[79] Smith M 2024 SIMULIA/Abaqus® 6.6 Manual
[80] Pozniak A A, Smardzewski J and Wojciechowski K W 2013 Computer simulations of auxetic foams in two dimensions *Smart Mater. Struct.* **22** 084009

[81] Mizzi L, Attard D, Gatt R, Dudek K K, Ellul B and Grima J N 2020 Implementation of periodic boundary conditions for loading of mechanical metamaterials and other complex geometric microstructures using finite element analysis *Eng. Comput.* **37** 1765–79
[82] Zhang Q, Yu X, Xia Y, Zhang D, Lakes R S, Wojciechowski K W and Scarpa F 2024 The shear performance of uniaxially thermoformed auxetic polymer foams *Composites* B **286** 111791
[83] Wu W, Owino J, Al-Ostaz A and Cai L 2014 Applying periodic boundary conditions in finite element analysis *SIMULIA community conf.* (*Providence*) pp 707–19
[84] Lempriere B M 1968 Poisson's ratio in orthotropic materials *AIAA J.* **6** 2226–7
[85] Mentrasti L, Molari L and Fabiani M 2021 Poisson's ratio bounds in orthotropic materials. Application to natural composites: wood, bamboo and Arundo donax *Composites* B **209** 108612
[86] Gatt R, Attard D, Farrugia P-S, Azzopardi K M, Mizzi L, Brincat J-P and Grima J N 2013 A realistic generic model for anti-tetrachiral systems *Phys. Status Solidi* b **250** 2012–9
[87] Mizzi L, Azzopardi K M, Attard D, Grima J N and Gatt R 2015 Auxetic metamaterials exhibiting giant negative Poisson's ratios *Phys. Rapid Res. Ltrs* **9** 425–30